JOURNAL OF PROPULSION AND POWER
Vol. 17, No. 6, November–December 2001

Thermal Analysis of Fluid-Structural Interaction in High-Speed Engine Flowfields

Birgit U. Reinartz*
University of Technology Aachen, 52062 Aachen, Germany
and
Wolfgang W. Koschel†
DLR, German Aerospace Center, 74239 Hardthausen, Germany

The impetus toward development of a hydrogen-fueled scramjet engine to accelerate aerospace vehicles at hypersonic speeds has focused attention on the need to model accurately the fluid–thermal–structural interaction of such engines. The proposed method is able to solve coupled thermal problems by computing high-speed turbulent and compressible flowfields including multidimensional heat conduction in adjacent walls. To achieve a completely conservative coupling at the fluid–structural interface, the same finite element method is applied to both the fluid and the structural equations. The use of the surface energy-balance equation with the boundary integral formulation yields a stable solution procedure for steady-state computations of the stiff problem. For the computation of the heat transfer inside a supersonic combustion chamber, the nonreactive gas flow solver is extended by an energy source term to simulate the heat addition due to the combustion process. The code is tested and applied to a combustor and test conditions experimentally investigated within the framework of the joint German–Russian cooperation on scramjet technology.

Nomenclature

a	=	speed of sound
c_p	=	specific heat at constant pressure
D	=	damping operator
E	=	total energy
e	=	specific energy
F	=	viewing factor for surface radiation
F_β	=	flux in direction of β
g_{O_2}	=	mass fraction of oxygen
H	=	source term
h	=	specific enthalpy
h	=	heat transfer coefficient
k	=	turbulent kinetic energy
M	=	Mach number
$\boldsymbol{M}$	=	mass matrix
$\boldsymbol{M}_L$	=	lumped mass matrix
N	=	form function
Pr	=	Prandtl number
p	=	pressure
q	=	turbulent velocity
$\dot{q}$	=	heat flux density
R	=	specific gas constant
Re	=	Reynolds number
S_e	=	element pressure switch
$S_{\alpha\beta}$	=	velocity gradient tensor
T	=	temperature
U	=	conserved variables
u_α	=	velocity component in direction of α
x_α	=	Cartesian coordinates
Γ	=	computational boundary
$\delta_{\alpha\beta}$	=	Kronecker delta
$\epsilon_s\sigma$	=	radiation emission coefficient times Stefan–Boltzmann constant
κ	=	isentropic exponent
λ	=	thermal conductivity
μ	=	viscosity
ν	=	Runge–Kutta level
ρ	=	density
σ	=	stress tensor
Ω	=	computational domain
ω	=	specific rate of turbulent diffusion

Subscripts and Superscripts

d	=	diffusive
e	=	element
F	=	fluid
I, J	=	global node number
i, j	=	local element node number
k	=	convective
S	=	structure
t	=	turbulent
$\bar{u}$	=	Reynolds-averaged variable u
$\tilde{u}$	=	Favre-averaged variable u
u''	=	turbulent fluctuation of variable u
w	=	wall
$,\beta$	=	partial derivative with respect to x_β

Introduction

THE high demands on the capability and performance of future engine components promote the development of new analysis and design methods for engine systems. Those methods combine classically separated fields of interest such as aerodynamic and structural analyses to reduce the margin of error introduced by the analysis. Until recently, combined methods of solution for fluid–structural interaction have mainly been applied to the sizing of the thermal protection system,[1] to improving the prediction of heat resistance for turbine blades,[2] or to the analysis of thermal loads on nose configurations.[3] The renewed interest in hypersonic vehicles has spurred the development of numerical analysis tools for internal supersonic engine flows. Because of the high flow velocity, the aerodynamic heating and the combustion temperature cause an intense thermal load to the engine structure, which needs to be studied.

Received 25 June 2000; revision received 17 January 2001; accepted for publication 4 March 2001.

*Research Engineer, Institute of Mechanics, Templergraben 64; birgit@lufmech.rwth-aachen.de. Student Member AIAA.

†Professor, Institute for Space Propulsion, DLR Lampoldshausen, Langer Grund; wolfgang.koschel@dlr.de. Senior Member AIAA.

Within the framework of the joint German–Russian cooperation on scramjet technology, a supersonic combustor with variable geometry was experimentally investigated under different test conditions. One point of interest was the determination of engine heat loads to identify favorable design features and material requirements leading to new engine concepts. Because the accurate experimental determination of wall heat fluxes in high-speed flows is marked with difficulties and can only provide measurements for a few discrete locations, a comparison with a numerical simulation was attempted. The presented numerical analysis tool combines the computation of the flowfield inside the combustor with the multidimensional heat conduction in the engine structure to compute the experimentally determined thermal loads. A finite element analysis is applied to both sets of equations, fluid and structural, to obtain a conservative solution for the thermal interaction without the necessity of specifying the unknown wall temperatures and, therefore, allowing the accurate computation of the wall heat fluxes. A one-dimensional scramjet combustion model is applied to determine the heat addition due to the combustion process, and the nonreactive gas flow equations are extended by the determined energy source term to account for the combustion.

Governing Equation

Flow Equations

The Favre-averaged conservation equations for a compressible ideal gas flow are applied to the fluid portion of the computational domain

$$\frac{\partial \boldsymbol{U}}{\partial t} + \left(\boldsymbol{F}^k_\beta - \boldsymbol{F}^d_\beta\right)_{,\beta} = \boldsymbol{H} \tag{1}$$

where the averaged conservation variables are

$$\boldsymbol{U} = [\bar{\rho}, \bar{\rho}\tilde{u}_\alpha, \bar{\rho}\tilde{E}]^T \tag{2}$$

and $\boldsymbol{H}$ represents a source term. The convective and diffusive fluxes are

$$\boldsymbol{F}^k_\beta = \begin{pmatrix} \bar{\rho}\tilde{u}_\beta \\ \bar{\rho}\tilde{u}_\alpha\tilde{u}_\beta + \bar{p}\delta_{\alpha\beta} \\ \tilde{u}_\beta(\bar{\rho}\tilde{E} + \bar{p}) \end{pmatrix} \tag{3}$$

and

$$\boldsymbol{F}^d_\beta = \begin{pmatrix} 0 \\ \bar{\sigma}_{\alpha\beta} - \overline{\rho u''_\alpha u''_\beta} \\ \tilde{u}_\alpha\bar{\sigma}_{\alpha\beta} - \bar{\dot{q}}_\beta - \overline{\rho u''_\beta h''} - \overline{\rho u''_\beta u''_\alpha u''_\alpha} \end{pmatrix} \tag{4}$$

respectively. The averaging of the total energy by Favre

$$\tilde{E} = \tilde{e} + \tfrac{1}{2}\cdot\tilde{u}_\alpha\tilde{u}_\alpha + \overline{\rho u''_\alpha u''_\alpha}/\bar{\rho} \tag{5}$$

yields the contribution of the turbulent kinetic energy

$$k := \tfrac{1}{2}\cdot\overline{\rho u''_\alpha u''_\alpha}/\bar{\rho} \tag{6}$$

to the total energy. The Newton stress tensor is a linear function of the velocity gradients tensor with μ being the proportionality constant

$$\bar{\sigma}_{\alpha\beta} = \mu\cdot\bar{S}_{\alpha\beta} \tag{7}$$

where

$$\bar{S}_{\alpha\beta} = (\tilde{u}_{\alpha,\beta} + \tilde{u}_{\beta,\alpha}) - \tfrac{2}{3}\delta_{\alpha\beta}\tilde{u}_{\gamma,\gamma} \tag{8}$$

Applying Fourier's law, the heat flux is a linear function of the temperature gradient

$$\bar{\dot{q}}_\beta = -\lambda_F\cdot\bar{T}_{,\beta} \tag{9}$$

The fluid is assumed as a calorically perfect-gas flow with the thermal equation of state

$$\bar{p}/\bar{\rho} = R\cdot\bar{T} \tag{10}$$

and a constant isentropic exponent for air of $\kappa = 1.4$. The temperature dependency of the molecular viscosity is considered by Sutherland's empirical equation

$$\mu = \mu_{\text{ref}}\cdot(T_{\text{ref}} + S)/(T + S)\cdot(T/T_{\text{ref}})^{1.5} \tag{11}$$

with $\mu_{\text{ref}} = 1.7156\cdot10^{-5}$ kg/m·s, $T_{\text{ref}} = 273.15$ K, and $S = 110$ K. The thermal conductivity of the fluid is determined assuming a constant Prandtl number of $Pr = 0.72$,

$$\lambda_F = c_p\cdot\mu/Pr \tag{12}$$

To model the additional correlation terms, an eddy viscosity model is applied where the correlations are substituted by relations of the gradients of the averaged conservation variables and turbulent transport coefficients. The Reynolds stresses are denoted as

$$-\overline{\rho u''_\alpha u''_\beta} = \mu_t\bar{S}_{\alpha\beta} - \tfrac{2}{3}\delta_{\alpha\beta}\bar{\rho}k \tag{13}$$

The diffusion of total energy by the turbulent motion is expressed as turbulent heat flux,

$$-\overline{\rho u''_\beta h''} = \frac{\mu_t}{Pr_t}\cdot\frac{\partial\tilde{h}}{\partial x_\beta} \tag{14}$$

where the turbulent Prandtl number is considered constant ($Pr_t = 0.9$). Finally, the turbulent flux of the Reynolds stresses is presented by the gradient of the turbulent kinetic energy,

$$-\overline{\rho u''_\beta u''_\alpha u''_\alpha} = \frac{\mu_t}{Pr_k}\cdot\frac{\partial k}{\partial x_\beta} \tag{15}$$

Therefore, only the turbulent energy k and the turbulent viscosity μ_t remain to be determined by the turbulence model to close the conservation equations of the fluid.

Structural Equation

Within the structure, the conservation equations (1) reduce to the heat transfer equation

$$\frac{\partial \boldsymbol{U}_S}{\partial t} + \left(\boldsymbol{F}^d_{\beta S}\right)_{,\beta} = 0 \tag{16}$$

with

$$\boldsymbol{U}_S = \rho_S c_S T_S, \qquad \boldsymbol{F}^d_{\beta S} = \dot{q}_{\beta S} \tag{17}$$

where c_S is the specific heat capacity. Inside the wall, only Fourier heat conduction (9) is of importance (radiation and convection being solely considered within the boundary conditions). The thermal conductivity and the specific heat capacity of the structure are determined by interpolation of temperature-dependent material properties using the Aitken algorithm (see Ref. 4).

Fluid–Structural Interface

Along the fluid–structural interface, the continuity of the energy fluxes has to be ensured, whereas the energy and the transport coefficients show a discontinuity of some orders of magnitude. Therefore, the thermal coupling yields a stiff system of equations, and numerical stability is a major concern. During each iteration, first the flowfield is computed using the structural wall temperature as interface boundary condition, and then the structural equations are solved using the latest known information from the other zone and including the surface energy balance along the interface

$$h\cdot(T_{\text{ref}} - T_w) + \dot{q}_{r,\text{gas}} = \dot{q}_{\text{cond}} + F\cdot\epsilon_S\sigma T^4_w \tag{18}$$

The left-hand side contains the convective heat transfer and the gas radiation of the fluid and the right-hand side expresses the structural heat conduction and the radiation of the combustor wall. For stability reasons, the fluid convective heat transfer is defined as the product of the heat transfer coefficient h and a temperature difference, where T_{ref} is not the recovery temperature but the fluid temperature computed in the node adjacent to the wall. This formulation turned out to be more stable than inserting the computed convective heat transfer directly[1] because h is not fluctuating quite as strongly and

the reference temperature formulation makes the temperature difference small and allows for a direct influence of the newly computed structural wall temperature. Because the same algorithm is applied to the fluid as well as to the structural conservation equations, the interface resolution is completely conservative, resulting in a stable and strongly coupled solution method.

Turbulence Modeling

To close the turbulent conservation equations (1) the low Reynolds number q–ω turbulence model suggested by Coakley and Huang[5] is applied. The model includes low Reynolds number damping functions, allowing the application of the model to separated boundary layer flows. The transport equations are

$$\frac{\partial \boldsymbol{U}_{q\omega}}{\partial t} + \left(\boldsymbol{F}^{k}_{\beta_{q\omega}} - \boldsymbol{F}^{d}_{\beta_{q\omega}}\right)_{,\beta} = \boldsymbol{H}_{q\omega} \tag{19}$$

with the conservation variables

$$\boldsymbol{U}_{q\omega} = \begin{pmatrix} \bar{\rho} q \\ \bar{\rho} \omega \end{pmatrix} \tag{20}$$

where ω is the specific rate of dissipation and $q = \sqrt{k}$. The turbulent fluxes

$$\boldsymbol{F}^{k}_{\beta_{q\omega}} = \begin{pmatrix} \bar{\rho} \tilde{u}_{\beta} q \\ \bar{\rho} \tilde{u}_{\beta} \omega \end{pmatrix} \tag{21}$$

and

$$\boldsymbol{F}^{d}_{\beta_{q\omega}} = \begin{bmatrix} \left(\mu + \dfrac{\mu_t}{\sigma_q}\right) \dfrac{\partial q}{\partial x_{\beta}} \\ \left(\mu + \dfrac{\mu_t}{\sigma_{\omega}}\right) \dfrac{\partial \omega}{\partial x_{\beta}} \end{bmatrix} \tag{22}$$

contain the usual convective and diffusive terms. The main emphasis of the model development is contained in the source term

$$\boldsymbol{H}_{q\omega} = \begin{bmatrix} C_{q1}\left[C_{\mu} D_q C_S - \frac{2}{3}(\tilde{u}_{\gamma,\gamma}/\omega) - C_{M_t}\right] \bar{\rho} \omega q \\ C_{\omega 1}[C_{\mu} C_S - C_{\omega 3}(\tilde{u}_{\gamma,\gamma}/\omega) - C_{\omega 2}/C_{\omega 1}] \bar{\rho} \omega^2 \end{bmatrix} \tag{23}$$

with the following abbreviations:

$$C_S = (\bar{S}_{\alpha\beta} \cdot \tilde{u}_{\alpha,\beta}) \big/ \omega^2, \qquad C_{M_t} = \left(1 + M_t^2\right)$$

The damping functions D_q and $C_{\omega 1}$

$$D_q = 1 - \exp(-\alpha_{q\omega} Re_t), \qquad C_{\omega 1} = 0.5 D_q + 0.055 \tag{24}$$

act on low Reynolds number flow portions with the turbulent Reynolds number

$$Re_t = \bar{\rho} q y_p / \mu \tag{25}$$

where y_p is the minimum wall distance. The introduction of the turbulent Mach number

$$M_t = \sqrt{2} q \big/ a \tag{26}$$

in the source term corresponds to the Sarkar et al. model[6] to take compressibility effects into account. This model addition is necessary for the computation of shock/boundary-layer interaction. Furthermore, the model constants are

$$C_{q1} = 0.5, \qquad C_{\omega 2} = 0.833, \qquad C_{\omega 3} = 2.4, \qquad C_{\mu} = 0.09$$

$$\alpha_{q\omega} = 0.022, \qquad \sigma_q = 0.8, \qquad \sigma_{\omega} = 2.0 \tag{27}$$

The turbulent viscosity is determined as

$$\mu_t = C_{\mu} D_q (\bar{\rho} q^2 / \omega) \tag{28}$$

To improve the computation of wall heat fluxes, Coakley and Huang[5] propose a restriction on the turbulent length scale in the vicinity of the wall

$$l_t = \min(2.5 \cdot y_p, q/\omega) \qquad \text{for} \qquad y^+ \le 20 \tag{29}$$

resulting in an increasing specific rate of dissipation,

$$\omega = q / l_t \tag{30}$$

Thus, the coupled systems of equations (1) and (19) represent a closed system for computing turbulent compressible flows.

One-Dimensional Combustion Model

Because a nonreactive gas flow is considered, the heat addition due to the hydrogen combustion process is modeled by utilizing an energy source term obtained from a one-dimensional supersonic combustion model.[7] The overall heat addition is obtained from the following relation:

$$\dot{Q}_{\text{chem}} = \dot{m}_{\text{H}_2} \cdot \min(1; 1/\Phi) \cdot H_u \cdot f_{\text{mo}M} \tag{31}$$

where $\dot{m}_{\text{H}_2}$ is the fuel mass flow and the equivalence ratio is defined as $\Phi = \dot{m}_{\text{O}_2,\text{stoich}} / \dot{m}_{\text{O}_2}$. The lower heating value H_u of hydrogen depends on the injection temperature, and the distribution functions $f_{\text{mo}M}$ approximates the axial status of molecular mixing between air and fuel. The molecular mixing is assumed to be a chi-square approximation of the combustion efficiency, which is determined by empirical estimations of the mixing layer ratio and the equivalence ratio. For the current combustor, the combustion model yields an efficiency of 95% at the combustor outlet. In comparison, the combustion efficiency determined by the experiment (using a one-dimensional analytical model with the static pressure distribution as input) is 97% (Ref. 8). Furthermore, for the two-dimensional computations, a distribution of the heat addition in the normal direction is required. When it is assumed that the main heat addition due to combustion takes place in the center of the combustor, a standard normal distribution is chosen in the y direction. Because of the high flow velocities, the upstream influence of the energy source term is negligible, and the heat transfer by convection and conduction is small in the normal direction. Therefore, the main influence of the heat addition on the wall heat fluxes is due to the induced pressure rise.

Mesh Generation

The discretization for arbitrary-shaped computational domains is accomplished by an automatic mesh generation scheme using hybrid structured/unstructured elements.[9] The domain geometry is first described by segment functions followed by the description of a background grid specifying the mesh parameters such as element sizes and stretching factors. The automatic net generator creates the unstructured triangular elements and the corresponding nodes simultaneously by applying the advancing front method. For boundary layers in high Reynolds number flows, large grid aspect ratios are required to resolve the physical flow conditions. For those conditions, structured quadrilateral elements are better suited than unstructured grids in providing efficient discretization of the boundary layer. Therefore, on body surfaces, an advancing layer method is applied to yield boundary-layer discretization. Finally, different optimization procedures are used to improve the mesh quality. The automatic mesh generator offers the ability to improve the computation by solution-adapted remeshing of the grid. An error indicator is computed from one or more specified solution variables followed by a complete regeneration of the grid based on the analysis of the error indicator.

For the combined fluid-structural thermal analysis, the mesh generator is first applied to the flow domain because this is usually the more restrictive part of the computational domain in terms of element size and node distribution. Then interface nodes are used as fixed boundary condition for generating the structural grid with pure unstructured triangles. Both domains share the same nodes along the interface, thus enabling even closer coupling of the solutions.

Numerical Method

The spatial discretization of the conservation equations (1) and (16) are based on a Galerkin finite element algorithm (see Refs. 10 and 11)

$$\int_\Omega \frac{\Delta\hat{U}}{\Delta t} N \,\mathrm{d}\Omega + \int_\Omega (\hat{F}_\beta)_{,\beta} N \,\mathrm{d}\Omega = \int_\Omega \hat{H} N \,\mathrm{d}\Omega \tag{32}$$

where Ω represents the computational domain and N are the weighing functions. When linear and bilinear approximation functions N

$$\hat{U} = \sum_J U_J \cdot N_J, \qquad \hat{F} = \sum_J F_J \cdot N_J \tag{33}$$

are applied for the triangular and quadrilateral elements, respectively, the integral equation can be discretized as follows:

$$\sum_e \int_{\Omega_e} N_j N_i \,\mathrm{d}\Omega_e \cdot \frac{\Delta U_i}{\Delta t} = \sum_e \left[\int_{\Omega_e} (N_j)_{,\beta} N_i \,\mathrm{d}\Omega_e \cdot (F_\beta)_j - \int_{\Gamma_e} N_j N_i \,\mathrm{d}\Gamma_e \cdot (F_\beta)_j n_\beta + \int_{\Omega_e} N_j N_i \,\mathrm{d}\Omega_e \cdot H_j \right] \tag{34}$$

where Γ_e is the element boundary. The mass matrix is determined as

$$\boldsymbol{M} = \sum_e \int_{\Omega_e} N_j N_i \,\mathrm{d}\Omega_e \tag{35}$$

and, for relaxation toward steady state, the lumped mass matrix

$$(\boldsymbol{M}_L)_{II} = \sum_J \boldsymbol{M}_{IJ} \tag{36}$$

as well as a local time step are applicable. The relaxation toward steady state is achieved by a five-step Runge–Kutta scheme proposed by Jameson[12]

$$\boldsymbol{U}^{\nu+1} = \boldsymbol{U}^n + \alpha_\nu \Delta t \left[\boldsymbol{M}_L^{-1} R(\boldsymbol{U}^\nu) + D^{(2)}(\boldsymbol{U}^\mu) + D^{(4)}(\boldsymbol{U}^\mu) \right] \tag{37}$$

where

$$\nu = 0, \ldots, 4, \qquad \mu = \min(\nu, 1) \tag{38}$$

and $R(\boldsymbol{U}^n)$ is the right-hand side of Eq. (34). The Runge–Kutta coefficients correspond to maximum stability, thus reducing the time accuracy to second order. To avoid spurious oscillations and to achieve a stationary solution, a second- and a fourth-order damping term are required for the gas flow equations. $D^{(2)}$ represents a nonlinear shock-capturing term

$$D^{(2)} = c_d^{(2)} M_L^{-1} \sum_e \frac{S_e}{\Delta t_e} [M_e - (M_L)_e] \cdot U^n \tag{39}$$

where $c_d^{(2)}$ is a constant diffusion coefficient and S_e is a dimensionless pressure switch that varies between 0 and 1 from smooth flow to near discontinuous flow,

$$S_e = \frac{1}{(N_i)_e} \sum_{i=1}^{(N_i)_e} \left| \frac{\sum_e [M_e - (M_L)_e] p}{\sum_e |[M_e - (M_L)_e] p|} \right| \tag{40}$$

with $(N_i)_e = 3$ or 4. However, in case of shock/boundary-layer interaction, S_e might be close to 1 in areas where the physical viscosity is sufficient to obtain a smooth solution. Thus, S_e is multiplied by the local Mach number scaled with the reference Mach number of the inflow[13]

$$\tilde{S}_e = \begin{cases} S_e & S_e \geq \frac{1}{2} \cdot (S_e)_{\max} \\ S_e \cdot Ma/Ma_{\text{ref}} & S_e < \frac{1}{2} \cdot (S_e)_{\max} \end{cases} \tag{41}$$

$$D^{(4)} = M_L^{-1} \sum_e \frac{r^{(4)}}{\Delta t_e} [M_e - (M_L)_e] \times \left\{ M_L^{-1} \sum_e [M_e - (M_L)_e] \cdot U^n \right\} \tag{42}$$

denotes the high-frequency damping term necessary to obtain stationary solutions where $D^{(2)}$ is not active and

$$r^{(4)} = \max\left[0, c_d^{(4)} - c_d^{(2)} \cdot \tilde{S}_e\right] \tag{43}$$

Computational Results

Before the results of the simulation of the scramjet combustor are presented, two validation problems are discussed.

Turbulent Flow over Flat Plate

The first test case is a $M_\infty = 0.5$ flow ($Re_L = 9 \times 10^5$) over a cooled copper plate ($T_w/T_t = 0.8$) that has been experimentally analyzed by Rüd.[14] The lower side of the thin flat plate ($h = 0.045$ m) is held at a constant temperature of $T_w = 698.5$ K, and the conservation equations of fluid and structure are solved in a combined manner to yield the wall heat flux. Figure 1 shows the Stanton number distribution along the plate. Because there is no transition model incorporated in the flow equations, the turbulence model is active in the whole flowfield resulting in the observed starting behavior near the leading edge of the plate. Away from the leading edge, the computed solution converges rapidly toward the semi-empirical Stanton number relation (see Ref. 15). Also shown are the measurements obtained by Rüd[14] that yield a laminar flow in the front part of the plate. However, after the transition to turbulent flow, the agreement between computed and measured values is excellent. In Fig. 2, the dimensionless profiles of velocity ($u^+ = u/u_\tau$) and

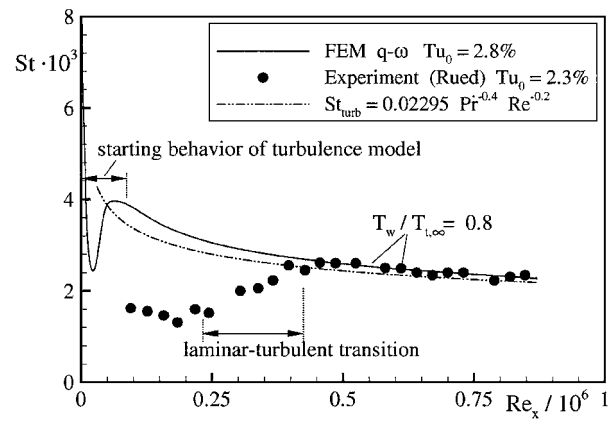

Fig. 1 Stanton number distribution for the computed flow over a cooled flat copper plate in comparison to experimental[14] and analytical results.

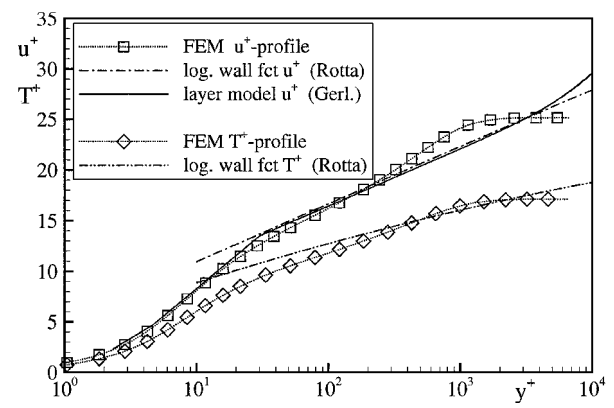

Fig. 2 Dimensionless boundary layer profile of temperature and velocity for the computed flow over a cooled flat copper plate in comparison to analytical results.[13,16]

temperature [$T^+ = (T - T_W)\rho_W c_p u_\tau / \dot{q}_W$] are compared to the logarithmic wall functions[16] and to a multilayer turbulent boundary profile.[13] To achieve an accurate computation of wall heat fluxes, it is essential that the turbulent profiles and wall gradients are determined correctly as shown in Fig. 2.

Wall Injection into Supersonic Flow

Next, the sonic injection of air into a supersonic main stream ($M_\infty = 3.75$, $Re_L = 2 \times 10^7$) is considered. This test case is based on an experiment performed by Aso et al.[17] on a flat plate with an injection slot ($d = 1$ mm). The experimental configuration was explicitly chosen to approximate a two-dimensional problem and to serve as computational validation problem. During the experiment, different ratios p^* of the total injection pressure to total freestream pressure were tested.

A schematic representation of the complex flowfield around a transverse injection is shown in Fig. 3. The injection induces a bow shock resulting in a strong pressure gradient, which causes the boundary layer to separate upstream of the injection slot. Inside the separation bubble, a primary and a counter-rotating secondary vortex develop. On exiting the nozzle, expansion of the jet is followed by a strong deceleration resulting in a sonic surface (Mach disk in three dimensions) at the top of the jet plume. Downstream of the injection, the boundary layer reattaches again, inducing a recompression shock. Depending on the size of the downstream separation bubble, there are one or more vortices contained in the bubble.

Figure 4 shows the hybrid grid applied to the computation after several remeshings. The first layer of grid points adjacent to the wall have a distance of $y^+ \leq 1$ to resolve the highly distorted boundary layer correctly. In Fig. 5, the corresponding Mach isolines for a pressure ratio p^* of 0.31 are presented. The different shocks and the two separation bubbles are clearly visible in the contour plot. Figure 6 yields the streamlines in the vicinity of the injection slot corresponding to the contour plot. Here, the two upstream and the primary and secondary downstream vortices become apparent.

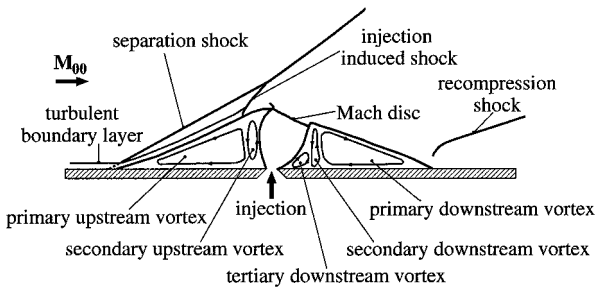

Fig. 3 Schematic representation of the flowfield around a sonic wall injection into a supersonic main stream causing shock/shock and shock/boundary-layer interaction.

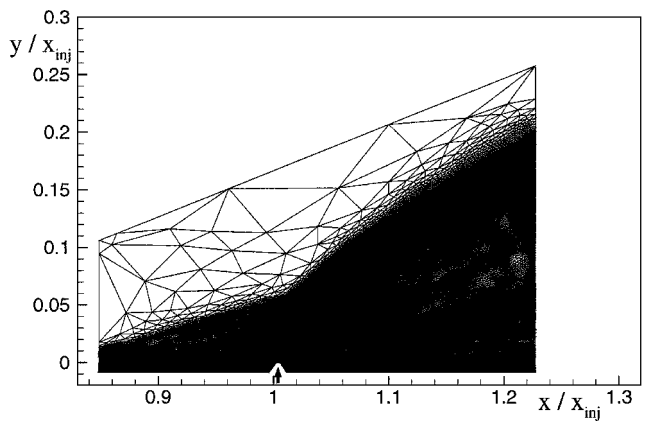

Fig. 4 Hybrid mesh with 43,100 nodes for the computation of transversal sonic injection into a supersonic flow after several solution-adapted remeshings.

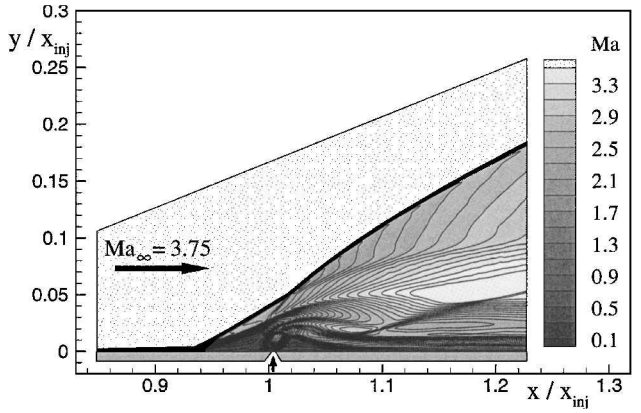

Fig. 5 Mach isolines for transversal sonic injection with a pressure ratio of $p^* = 0.31$.

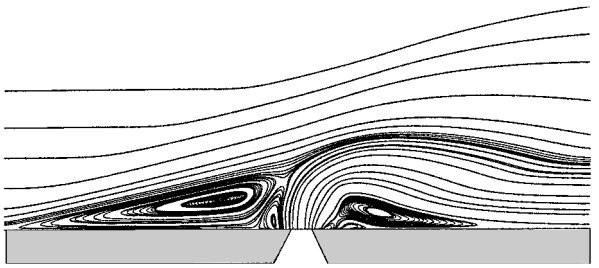

Fig. 6 Streamlines in the vicinity of the injection slot.

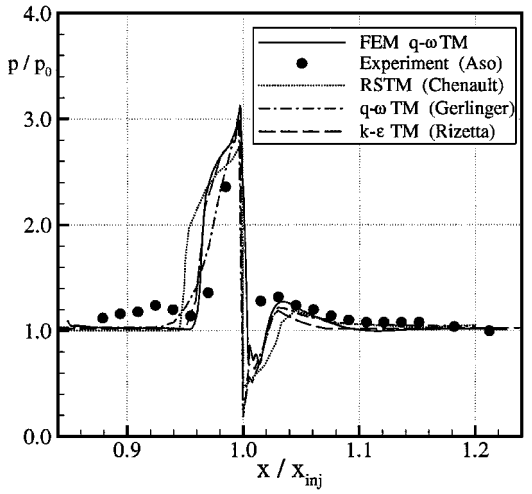

Fig. 7 Wall pressure distributions for total pressure ratio $p^* = 0.085$ in comparison to several results from literature.[13,17,19,20]

The tertiary downstream vortex is barely visible but is mandated by the direction of the flow.

Because the experiment performed by Aso et al.[17] is considered as a two-dimensional test case, there are many different numerical comparisons found in the literature. In Figs. 7 and 8, the computed wall pressure distributions for two different injection pressures are compared to the experimental data, as well as to previously reported computations including an algebraic turbulence model,[18] two two-equations models,[13,19] and a Reynolds stress turbulence model.[20] The separation of the boundary layer is marked by a strong pressure gradient followed by a pressure plateau corresponding to the relatively constant flow conditions inside the upstream bubble. The pressure peak is caused by the conjunction of primary and secondary vortices. Downstream of injection, a pressure minimum is reached that rapidly rises toward a relative maximum in the vicinity of the recompression shock. The experimental values show a pressure rise before separation that is caused by unsteady inflow conditions and spillage.[19,20] In addition, the experimental measurements miss the

pressure peak caused by the two upstream vortices due to an insufficient number of pressure tabs. However, the existence of the maximum is supported by all computations presented as well as other measurements.[21]

Supersonic Combustion Chamber

The experimental combustor configuration investigated in the framework of the German–Russian cooperation on scramjet technology[8] is presented in Fig. 9. The inlet flow conditions of the test case analyzed in the computation are $M_\infty = 3.0$, $p_t = 2.33$ MPa, and $T_t = 1701$ K. The incoming air mass flow is 1.6 kg/s and was heated by precombustion ($g_{O_2} = 0.25$). Gaseous hydrogen was injected for 5 s at a sonic velocity of 1180 m/s and with a temperature of 280 K at the first injector location.

In the ideal-gas computation, the injection is simulated by a cold air jet with the same enthalpy flux as the hydrogen injection ($M_{inj} = 1.05$, $p_{t,inj} = 1.6$ MPa). The combustor structure consists of a 16-mm-thick CrNi–steel wall, which is not cooled during the experiment and, for the steady-state computations, is kept at a constant ambient temperature of 300 K at the outside. Figures 10 and 11 show the computed temperature distributions in the lower-half of the symmetric combustion chamber and combustor wall. The fluid–structural interface is marked by the developing temperature boundary layer. In case of injection, the wall downstream of the injector is cooled by the cold injected air. In addition, the nodes along the interface located inside the injector are kept at the constant injection temperature of 280 K, thus functioning as a heat sink for the surrounding domain. In Fig. 12, the wall temperature shows a very inhomogeneous distribution along the combustor that can only be obtained by a coupled solution method without predetermined energy boundary condition. The computational grid in the vicinity of the injection (marked by two bars) is shown in Fig. 13. The corresponding Mach number contours are presented in Fig. 14. Here, the domain is mirrored along the symmetry line to enhance the presentation of the Mach reflection caused by the two separation shocks. Behind the Mach reflection, there is a small domain of subsonic flow caused by the flow blockage due to the transversal jets. However, the flow rapidly accelerates again and reattaches downstream of the injection.

During the experiment, static wall pressure and wall heat fluxes were measured by pressure taps and differential thermocouples, respectively. Figures 15 and 16 yield the computed wall pressure

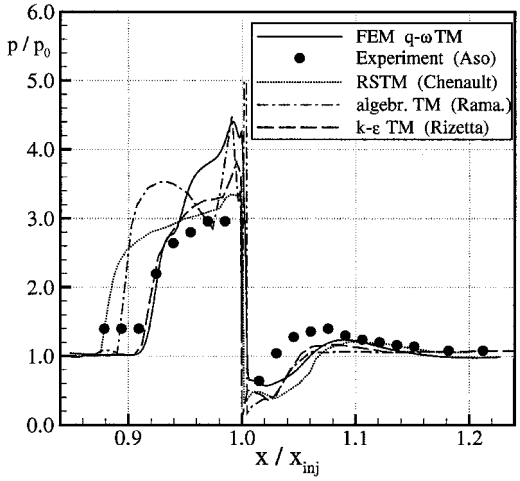

Fig. 8 Wall pressure distribution for total pressure ratio $p^* = 0.31$ in comparison to several results from literature.[17–20]

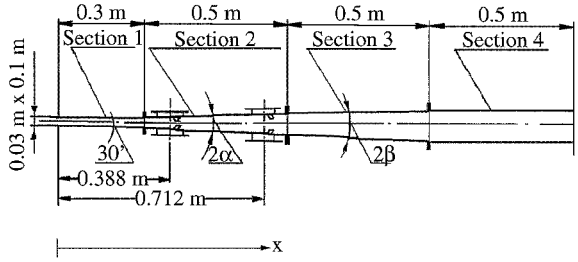

Fig. 9 Variable scramjet combustor geometry tested in the framework of the German–Russian cooperation with adjustable diverging angles ($\alpha = 1$ and 2 deg, $\beta = 0$ and 1 deg) and two injection locations ($x_{inj} = 0.388, 0.712$ m).

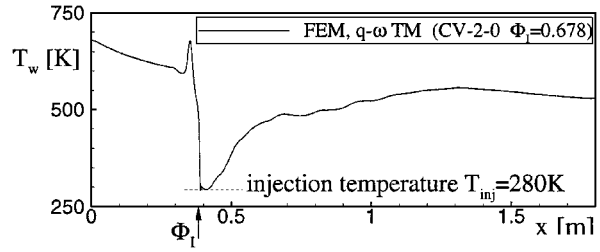

Fig. 12 Distribution of the wall temperature along the combustor length.

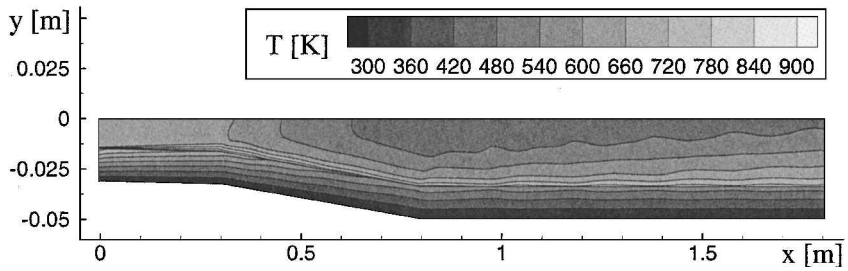

Fig. 10 Temperature contour plot (without injection) for the lower-half of the combustion chamber with a 16-mm-thick wall made of CrNi–steel (x–y ratio: 1:5).

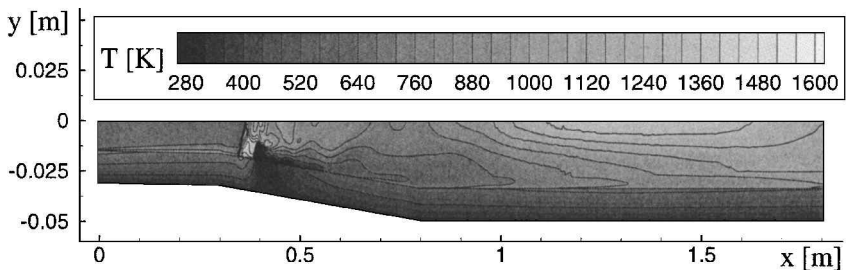

Fig. 11 Temperature contour plot with injection for the lower-half of the combustion chamber with a 16-mm-thick wall made of CrNi–steel (x–y ratio: 1:5).

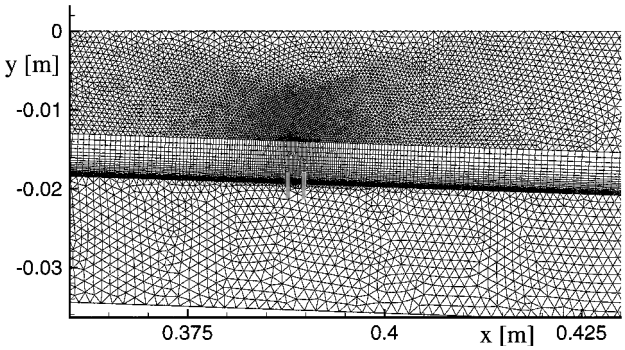

Fig. 13 Hybrid grid in the vicinity of the injection slot (marked by two vertical bars) with the combustor wall (lower section of unstructured triangular elements) as well as the boundary-layer region (structured quadrilaterals), and the inviscid flow portion (upper section of unstructured triangles).

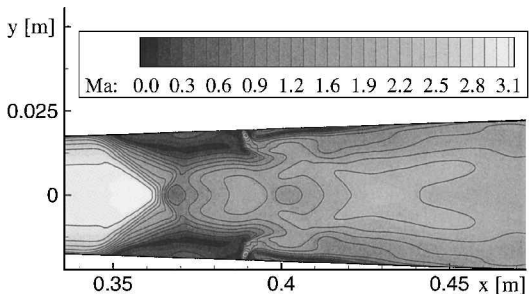

Fig. 14 Mach number contour plot of the injection area mirrored along the symmetry line.

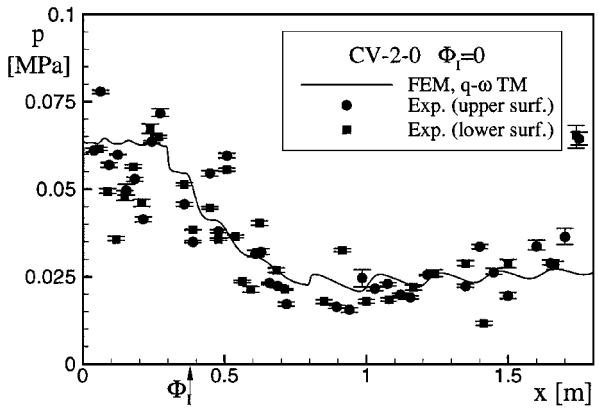

Fig. 15 Distribution of the computed wall pressure along the combustor length in comparison to the measurements.

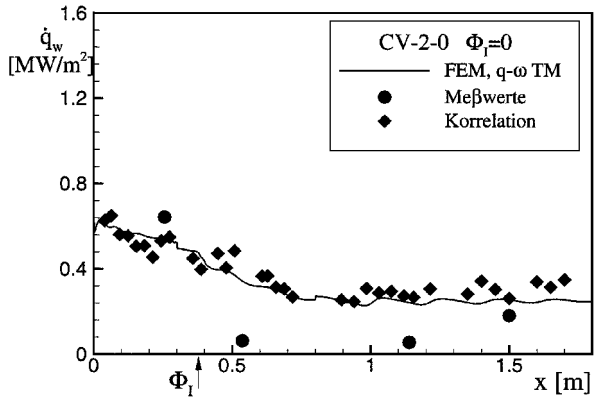

Fig. 16 Distribution of the wall heat flux along the combustor length in comparison to the measurements and a heat flux prediction method determined from the experimental pressure correlation[22] for aerodynamic heating.

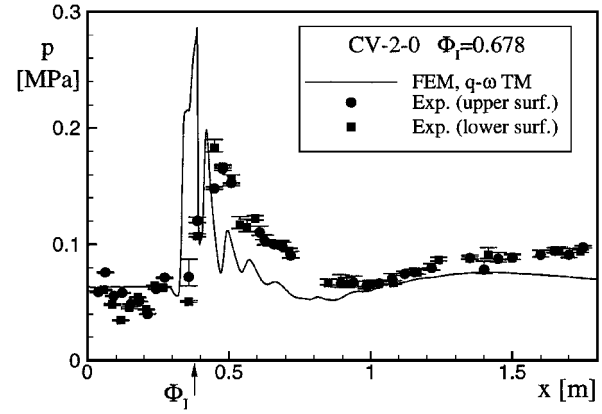

Fig. 17 Distribution of the wall pressure along the combustor length in comparison to the experimental measurements with fuel injection.

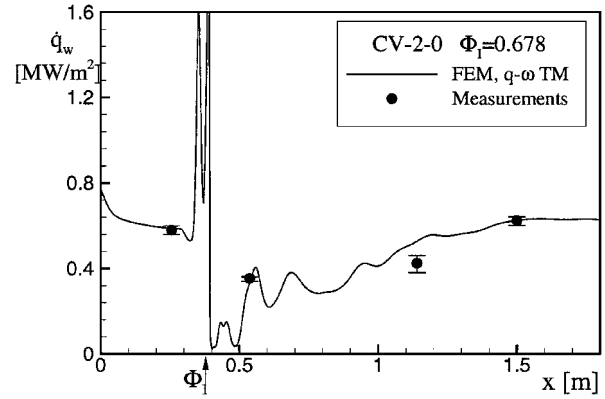

Fig. 18 Distribution of the wall heat flux along the combustor length in comparison to the experimental measurements with fuel injection.

and wall heat flux distribution for pure aerodynamic heating without injection. The wave distribution is caused by expansion waves resulting from the different diverging angles of the combustor. In comparison, the scattering of the experimental data is high, especially in the front part, where the injector induces separation. However, the error bars presenting graphically the minimum and maximum of five subsequent pressure measurements show that the flowfield itself is steady. The measured expansion corresponding to the diverging section of the combustor as well as the subsequent compression are in good agreement with the computed distribution. The measured heat flux distribution shows an unexplained decrease in the diverging section of the combustor not present in either the computation or the heat flux predictions obtained by the compressible Reynolds analogy and the experimental pressure data (see Ref. 22). Figures 17 and 18 present the wall distributions for the case of combustion. The injection results in the typical pressure peak distribution with subsequent reflection of the pressure peak at the opposite wall. The steady pressure rise in the constant combustor section is caused by the heat addition due to combustion. The experimental pressure distribution is the average of three measurement series, and again the error bars indicate a steady flow behavior. The wall heat fluxes compare favorably with the experimental data, also obtained by three subsequent measurements. A comparison with results of the correlation method is not shown because the method cannot account for the heat sink due to the cold injected air and the heat addition due to combustion. The two peak fluxes upstream of the injector correlate with the steep pressure rise due to separation and the peak pressure due to the conjunction of the two upstream vortices, respectively. Downstream of the injection, the wall heat flux is strongly reduced by the cold air injected in the main flow.

Conclusion

A coupled fluid–structural solver has been successfully applied to compute turbulent heat fluxes along diabatic walls including

shock/shock and shock/boundary-layer interaction, as well as transverse wall injection. Although the applied program package considers only two-dimensional effects, the computation of the thermal load of the modeled scramjet combustor approximates the experimental results closely. Therefore, the main flow features such as heat addition due to combustion and heat loss due to the cold injection are modeled correctly by the nonreactive solver. The conjugate algorithm for thermal interaction between fluid and structure presents a new advanced prediction method for thermal loads on high-speed engine components needed for improved computational engine design studies.

Acknowledgments

The authors acknowledge the financial support of this work by the Deutsche Forschungsgemeinschaft within the framework of the postgraduate program Transport Processes in Hypersonic Flows at the University of Technology Aachen.

References

[1]Milos, F., Chen, Y.-K., and Henline, W. D., "Methodology for Full-Body TPS Sizing of Access-to-Space Vehicles," AIAA Paper 96-0614, Jan. 1996.

[2]Imlay, S. T., Soetrisno, M., and Roberts, D. W., "Coupled Flow and Heat Transfer Analysis Using Hybrid Structured–Unstructured Grids," AIAA Paper 96-0622, Jan. 1996.

[3]Dechaumphai, P., Thornton, E. A., and Wieting, A. R., "Flow–Thermal–Structural Study of Aerodynamically Heated Leading Edges," *Journal of Spacecraft and Rockets*, Vol. 26, No. 4, 1989, pp. 201–209.

[4]Schwarz, H. R., "Interpolation nach Aitken-Nevill," *Numerische Mathematik*, 4th ed., B. G. Teubner, Stuttgart, Germany, 1986, pp. 130–139.

[5]Coakley, T. J., and Huang, P. G., "Turbulence Modeling for High Speed Flows," AIAA Paper 92-0436, Jan. 1992.

[6]Sarkar, S., Erlebacher, G., Hussaini, M. Y., and Kreiss, H. O., "The Analysis and Modelling of Dilatational Terms in Compressible Turbulence," *Journal of Fluid Mechanics*, Vol. 227, 1991, pp. 473–493.

[7]Kremer, F., "Eindimensionale Brennkammerbetrachtung für ein Staustrahltriebwerk mit Überschallverbrennung," German Aerospace Center, DLR Forschungsbericht 94-06, Cologne, Germany, Feb. 1994.

[8]Walther, R., Koschel, W., Sabelnikov, V., Korontsvit, Y., and Ivanov, V., "Investigations into the Aerothermodynamic Characteristics of Scramjet Components," International Symposium on Air Breathing Engines, ISABE Paper 97-7085, Sept. 1997.

[9]Bikker, S., Greza, H., and Koschel, W., "Parallel Computing and Multigrid Solution on Adaptive Unstructured Meshes," *Notes on Numerical Fluid Mechanics*, Vol. 47, No. 2, 1994, pp. 148–154.

[10]Koschel, W. W., Rick, W., and Bikker, S., "Application of Finite Element Method to Hypersonic Nozzle Flow Computation," *Proceedings of 77th AGARD PEP Symposium on CFD Techniques for Propulsion Applications*, May 1991, pp. 33/11–33/14.

[11]Morgan, K., and Peraire, J., "Finite Element Methods for Compressible Flows," von Kármán Inst., VKI Lecture Series, Rhode-Saint-Genese, Belgium, 1987, pp. 1–114.

[12]Jameson, A., "Positive Schemes and Shock Modelling for Compressible Flows," *International Journal for Numerical Methods in Fluids*, Vol. 20, No. 8–9, 1995, pp. 743–776.

[13]Gerlinger, P., "Numerische Berechnung turbulenter Verbrennungsvorgänge mit einem impliziten LU-Verfahren," VDI Fortschrittberichte, Reihe 7, Nr. 275, Verein Deutscher Ingenieure Verlag, Düsseldorf, Germany, 1995.

[14]Rüd, K., "Transitionale Grenzschichten," Ph.D. Dissertation, Dept. of Mechanical Engineering, Univ. Karlsruhe, Karlsruhe, Germany, June 1985.

[15]Kays, W. M., and Crawford, M. E., "Heat Transfer: The Turbulent Boundary-Layer," *Convective Heat and Mass Transfer*, 3rd ed., McGraw–Hill, New York, 1993, pp. 255–310.

[16]Rotta, J., "Über den Einfluß der Machschen Zahl und des Wärmeübergangs auf das Wandgesetz turbulenter Strömungen," *Zeitung für Flugwissenschaft*, Vol. 7, No. 9, 1959, pp. 264–274.

[17]Aso, S., Okuyama, S., Kawai, M., and Ando, Y., "Experimental Study on Mixing Phenomena in Supersonic Flows with Slot Injection," AIAA Paper 91-0016, Jan. 1991.

[18]Ramakrishnan, R., and Singh, D. J., "Modeling Scramjet Combustor Flowfields with a Grid Adaption Scheme," *AIAA Journal*, Vol. 32, No. 5, 1994, pp. 930–935.

[19]Rizzetta, D. P., "Numerical Simulation of Slot Injection into a Turbulent Supersonic Stream," *AIAA Journal*, Vol. 30, No. 10, 1992, pp. 2434–2439.

[20]Chenault, C. F., and Beran, P. S., "K-ϵ and Reynolds Stress Turbulence Model Comparisons for Two-Dimensional Injection Flows," *AIAA Journal*, Vol. 36, No. 8, 1998, pp. 1401–1412.

[21]Werle, M. J., Driftmyer, R. T., and Shaffer, D. G., "Jet-Interaction-Induced Separation: The Two-Dimensional Problem," *AIAA Journal*, Vol. 10, No. 2, 1972, pp. 188–193.

[22]Jürgens, B. U., and Koschel, W. W., "Thermal Load on a Scramjet Combustion Chamber," *Proceedings of 10th International Conference on Finite Elements in Fluids*, edited by M. Hafez, Softbound ed., Tucson, Jan. 1998, pp. 425–430.